bioRxiv preprint doi: https://doi.org/10.1101/2021.11.15.468761; this version posted November 17, 2021. The copyright holder for this preprint (which was not certified by peer review) is the author/funder, who has granted bioRxiv a license to display the preprint in perpetuity. It is made available under aCC-BY-NC-ND 4.0 International license.

1 # Microglia do not restrict SARS-CoV-2 replication following
2 infection of the central nervous system of K18-hACE2
3 transgenic mice
4
5 **Running Title: SARS-CoV-2 infection of the CNS**
6
7 Gema M. Olivarria[1*], Yuting Cheng[2*], Susana Furman[1*], Collin Pachow[2], Lindsay A. Hohsfield[1],
8 Charlene Smith-Geater[3], Ricardo Miramontes[4], Jie Wu[5], Mara S. Burns[1], Kate I. Tsourmas[1],
9 Jennifer Stocksdale[1], Cynthia Manlapaz[1], William H. Yong[6], John Teijaro[7], Robert Edwards[6],
10 Kim N. Green[1], Leslie M. Thompson[1,3,5,6], and Thomas E. Lane[1,2,8 #]
11
12 [1]Department of Neurobiology & Behavior, [2]Department of Molecular Biology & Biochemistry,
13 School of Biological Sciences, University of California, Irvine 92697
14
15 [3]Department of Psychiatry and Human Behavior, University of California, Irvine School of
16 Medicine, Irvine 92697
17
18 [4]Institute for Memory Impairments and Neurological Disorders, School of Biological Sciences,
19 University of California, Irvine 92697
20
21 [5]Department of Biological Chemistry, University of California, Irvine School of Medicine, Irvine
22 92697
23
24 [6]Department of Pathology & Laboratory Medicine, University of California, Irvine School of
25 Medicine, Irvine 92697
26
27 [7]Department of Immunology & Microbiology, The Scripps Research Institute, La Jolla CA
28 92037
29
30 [8]Center for Virus Research, University of California, Irvine 92697
31
32 *These authors contributed equally to this work
33
34 #Address Correspondence
35 Thomas E. Lane, Ph.D.
36 Department of Neurobiology & Behavior
37 School of Biological Sciences
38 University of California, Irvine
39 (949) 824-1360
40 Email: tlane@uci.edu
41
42
43
44

bioRxiv preprint doi: https://doi.org/10.1101/2021.11.15.468761; this version posted November 17, 2021. The copyright holder for this preprint (which was not certified by peer review) is the author/funder, who has granted bioRxiv a license to display the preprint in perpetuity. It is made available under aCC-BY-NC-ND 4.0 International license.

45 **Abstract**
46 Unlike SARS-CoV-1 and MERS-CoV, infection with SARS-CoV-2, the viral pathogen
47 responsible for COVID-19, is often associated with neurologic symptoms that range from mild to
48 severe, yet increasing evidence argues the virus does not exhibit extensive neuroinvasive
49 properties. We demonstrate SARS-CoV-2 can infect and replicate in human iPSC-derived
50 neurons and that infection shows limited anti-viral and inflammatory responses but increased
51 activation of EIF2 signaling following infection as determined by RNA sequencing. Intranasal
52 infection of K18 human ACE2 transgenic mice (K18-hACE2) with SARS-CoV-2 resulted in
53 lung pathology associated with viral replication and immune cell infiltration. In addition, ~50%
54 of infected mice exhibited CNS infection characterized by wide-spread viral replication in
55 neurons accompanied by increased expression of chemokine (*Cxcl9, Cxcl10, Ccl2, Ccl5* and
56 *Ccl19*) and cytokine (*Ifn-λ* and *Tnf-α*) transcripts associated with microgliosis and a
57 neuroinflammatory response consisting primarily of monocytes/macrophages. Microglia
58 depletion via administration of colony-stimulating factor 1 receptor inhibitor, PLX5622, in
59 SARS-CoV-2 infected mice did not affect survival or viral replication but did result in dampened
60 expression of proinflammatory cytokine/chemokine transcripts and a reduction in
61 monocyte/macrophage infiltration. These results argue that microglia are dispensable in terms of
62 controlling SARS-CoV-2 replication in in the K18-hACE2 model but do contribute to an
63 inflammatory response through expression of pro-inflammatory genes. Collectively, these
64 findings contribute to previous work demonstrating the ability of SARS-CoV-2 to infect neurons
65 as well as emphasizing the potential use of the K18-hACE2 model to study immunological and
66 neuropathological aspects related to SARS-CoV-2-induced neurologic disease.
67
68
69 **Keywords:** SARS-CoV-2, microglia, central nervous system, neuropathology
70
71 **Importance**
72 Understanding the immunological mechanisms contributing to both host defense and disease
73 following viral infection of the CNS is of critical importance given the increasing number of
74 viruses that are capable of infecting and replicating within the nervous system. With this in mind,
75 the present study was undertaken to evaluate the role of microglia in aiding in host defense
76 following experimental infection of the central nervous system (CNS) of K18-hACE2 with
77 SARS-CoV-2, the causative agent of COVID-19. Neurologic symptoms that range in severity are
78 common in COVID-19 patients and understanding immune responses that contribute to
79 restricting neurologic disease can provide important insight into better understanding
80 consequences associated with SARS-CoV-2 infection of the CNS.
81
82

bioRxiv preprint doi: https://doi.org/10.1101/2021.11.15.468761; this version posted November 17, 2021. The copyright holder for this preprint (which was not certified by peer review) is the author/funder, who has granted bioRxiv a license to display the preprint in perpetuity. It is made available under aCC-BY-NC-ND 4.0 International license.

83 **Introduction**

84 The clinical spectrum of COVID-19 is complex, and numerous risk factors and
85 comorbidities are considered important in affecting disease severity including age, obesity,
86 chronic respiratory disease, and cardiovascular disease [1]. In addition, neurological symptoms
87 are common in COVID-19 patients, suggesting the virus can potentially infect and replicate in
88 the central nervous system (CNS). Indeed, encephalitis and meningitis have been reported in
89 COVID-19 patients, and viral RNA and protein have been detected within the CSF of infected
90 patients [2-4]. Additionally, human brain organoids are susceptible to SARS-CoV-2 infection [2,
91 5], yet demonstration of extensive CNS penetrance by SARS-CoV-2 has remained elusive. It is
92 imperative to develop pre-clinical animal models of COVID-19 that capture consistent and
93 reproducible clinical and histologic readouts of many disease-associated symptoms following
94 experimental infection with clinical isolates of SARS-CoV-2 [6]. Importantly, these models
95 should be able to reliably evaluate interventional therapies to limit viral replication and mute
96 immune-mediated pathology, as well as evaluate effectiveness of novel vaccines, all while
97 remaining cost-effective. To date, the most common animal models employed to evaluate
98 COVID-19 pathogenesis include mice, non-human primates (rhesus macaques, cynomolgus
99 macaques and African green monkeys), Syrian hamsters, ferrets, and cats [6].

100 Human ACE2 (hACE2) transgenic mouse models have provided important insights into
101 the pathogenesis of COVID-19. Perlman and colleagues [7] developed the K18-hACE2 mice,
102 initially used as a mouse model of SARS-CoV-1, which has been successfully employed as a
103 model of COVID-19 [8]. Intranasal inoculation of SARS-CoV-2 in K18-hACE2 mice results in a
104 dose-dependent increase in weight loss and mortality with the lung being the major site of viral
105 infection, while lower amounts of virus are detected in the heart, liver, spleen, kidney, small

bioRxiv preprint doi: https://doi.org/10.1101/2021.11.15.468761; this version posted November 17, 2021. The copyright holder for this preprint (which was not certified by peer review) is the author/funder, who has granted bioRxiv a license to display the preprint in perpetuity. It is made available under aCC-BY-NC-ND 4.0 International license.

106 intestine, and colon [8]. Examination of lungs revealed distribution of viral antigen associated
107 with alveolar damage, interstitial lesions, edema, and inflammation. Lung infection resulted in an
108 increase in expression of interferons as well as inflammatory cytokines and chemokines
109 associated with neutrophil, macrophage/monocyte, and T cell infiltration. Viral RNA was also
110 detected within the sinonasal epithelium, and viral antigen was present in sustentacular cells
111 associated with anosmia [8]. Examination of brains of SARS-CoV-2 infected hACE2 transgenic
112 mice has indicated that infection of the CNS is not consistent, and in some cases, virus is rarely
113 detected [8-12]. This may reflect the SARS-CoV-2 isolate being studied as well as the dose of
114 virus being administered. However, in those animals in which virus penetrates the brain, there
115 can be extensive spread of the virus throughout different anatomic regions accompanied by cell
116 death [8], and these results are consistent with early studies examining SARS-CoV-1 infection of
117 K18-hACE2 mice [7]. High-level of CNS infection in K18-hACE2 is accompanied by meningeal
118 inflammation associated with immune cell infiltration into the brain parenchyma and microglia
119 activation [11]. Enhanced CNS penetrance and replication of SARS-CoV-2 within the CNS of
120 K18-hACE2 is associated with increased mortality; although the mechanisms by which this
121 occurs remain unclear. The present study was undertaken to i) expand on earlier studies
122 examining SARS-CoV-2 infection of human CNS resident cells, ii) evaluate the immune
123 response that occurs in response to SARS-CoV-2 infection of the CNS of K18-hACE2 mice and
124 iii) assess the contributions of microglia in host defense following CNS infection by SARS-CoV-
125 2.

126
127
128
129
130
131

bioRxiv preprint doi: https://doi.org/10.1101/2021.11.15.468761; this version posted November 17, 2021. The copyright holder for this preprint (which was not certified by peer review) is the author/funder, who has granted bioRxiv a license to display the preprint in perpetuity. It is made available under aCC-BY-NC-ND 4.0 International license.

132 **Results**
133
134 **SARS-CoV-2 infection of human neurons**. Previous studies have indicated neurons are
135 susceptible to infection by SARS-CoV-2 (2); therefore, we infected human iPSC-derived
136 neurons with SARS-CoV-2. Similar to earlier reports, SARS-CoV-2 was able to infect and
137 replicate within neurons as determined by staining for nucleocapsid protein (**Figures 1A and B**).
138 By 48h p.i., viral nucleocapsid protein had spread from the neuron cell body and extended down
139 dendritic and axonal projections (**Figures 1C and D**). Notably, we did not detect syncytia
140 formation in neuron cultures at any time following infection with SARS-CoV-2, suggesting that
141 virus may not spread via fusion with neighboring cells. RNA sequencing analysis revealed that
142 expression of both anti-viral and inflammatory responses in infected neurons was limited relative
143 to the genes within the heatmap at both 24h and 48h post-infection (**Figure 1E**). We then
144 evaluated pathways that may progressively change between 24h and 48h post-infection
145 comparing the Transcripts per million (TPMs) as input for Ingenuity Pathway Analysis (IPA).
146 **Figure 1F** shows the top 12 IPA canonical pathways that are overrepresented. eIF2 signaling is
147 the predominant pathway induced upon SARS-CoV-2 infection of neurons, followed by
148 pathways associated with oxidative phosphorylation, eIF4, MTOR signaling and mitochondrial
149 dysfunction, the latter with no prediction of activity. Notably, the Coronavirus Pathogenesis
150 Pathway is also overrepresented, however is inhibited in response to neuronal infection by
151 SARS-CoV-2 over the time frame tested with the majority of the genes represented encoding
152 ribosomal proteins (**Figure 1F**).
153
154 **SARS-CoV-2 infection of lungs of K18-hACE2 mice.** K18-hACE2 mice were intranasally
155 infected with either $1x10^4$, $5x10^4$ or $1x10^5$ plaque-forming units (PFU) of SARS-CoV-2, and

bioRxiv preprint doi: https://doi.org/10.1101/2021.11.15.468761; this version posted November 17, 2021. The copyright holder for this preprint (which was not certified by peer review) is the author/funder, who has granted bioRxiv a license to display the preprint in perpetuity. It is made available under aCC-BY-NC-ND 4.0 International license.

156 weight loss and mortality were recorded. Consistent with other reports [8-12], we observed a
157 general trend towards dose-dependent increase in weight loss and mortality out to day 7 post-
158 infection (p.i.) (**Figure 2A**). qPCR indicated the presence of viral RNA in lungs of infected K18-
159 hACE2 (**Figure 2B**). *In situ* hybridization of lungs of mice infected with $5x10^4$ PFU of virus at
160 day 7 p.i. revealed localized areas of viral infection as determined by expression of spike RNA
161 (**Figures 2C**). Hematoxylin and eosin staining of lungs demonstrated both alveolar and
162 interstitial lesions, with alveolar hemorrhage and edema (**Figures 2D**), interstitial congestion
163 (**Figure 2E**) and lymphocytic infiltrates (**Figure 2F**). qPCR analysis of proinflammatory
164 cytokines and chemokines indicated increased expression of *Ifn-λ, Cxcl10*, *Cxcr2*, and *Ccl2* yet
165 varied expression of *Il-10*, *TNF-α, Ccl19*, *and Ccl5* and limited expression of transcripts for *Ifn-*
166 *β1*(**Figure 2G**). Hematoxylin and eosin staining showed immune cell infiltrates in SARS-CoV-
167 2-infected lungs containing inflammatory CD8+ T cells as determined by immunofluorescent
168 staining (**Figures 3A-D**). In addition, germinal center-like structures were detected within the
169 lungs of SARS-CoV-2-infected mice with enriched CD8+ T cell accumulation (**Figures 3E and**
170 **F**). Collectively, our findings are consistent with previous studies employing SARS-CoV-2
171 infection of K18-hACE2 mice in terms of development of interstitial pneumonia and immune
172 cell infiltration associated with viral RNA present within the lungs [8-12].
173
174 **Neuroinvasion by SARS-CoV-2.** Following intranasal infection of mice with $5x10^4$ PFU of
175 SARS-CoV-2, virus was detected in the brain as determined by qPCR and RNAscope compared
176 to sham-infected mice (**Figures 4A-C**). Using a Spike-specific probe, we observed wide-spread
177 expansion of viral mRNA throughout the brain with many distinct anatomical regions infected as
178 well as spared. By day 7 p.i., viral RNA was present within the cortex (CTX), striatum (STR),

bioRxiv preprint doi: https://doi.org/10.1101/2021.11.15.468761; this version posted November 17, 2021. The copyright holder for this preprint (which was not certified by peer review) is the author/funder, who has granted bioRxiv a license to display the preprint in perpetuity. It is made available under aCC-BY-NC-ND 4.0 International license.

179 pallidum (PAL), thalamus (TH), hypothalamus (HY), midbrain (MB), pons (P), and medulla
180 (MD), whereas areas that were relatively spared included the olfactory bulb (OB), white matter
181 (WM) tracts, hippocampus (HC) and cerebellum (CB) (**Figure 4B**); no viral RNA was detected
182 in sham-infected K18-hACE2 mice (**Figure 4C**). Demyelinating lesions have been detected in
183 post-mortem brains of COVID-19 patients [13], however we did not detect any evidence of
184 demyelination within the brains of SARS-CoV-2-infected mice as determined by luxol-fast blue
185 (LFB) staining (**Figures 4D and E**). The predominant cellular target for SARS-CoV-2 infection
186 was neurons as determined by cellular morphology of cells positive for viral RNA (**Figures 5A**
187 **and B**). In a small percentage of infected mice, we were able to detect viral RNA in the olfactory
188 bulb with primary targets being mitral and glomerular neurons (**Figure 5C and D**). Prominent
189 neuropathological changes detected included perivascular cuffing (**Figure 5E**), subventricular
190 inflammation (**Figures 5F**) and leptomeningitis (**Figure 5G**), consistent with previous studies (2,
191 3).

192 Analysis of CNS myeloid cells showed increased IBA1 soma size and
193 shortened/thickened processes, indicative of microglial activation in SARS-CoV-2-infected mice
194 compared to sham-infected mice (**Figure 6A and B**). In addition, immunofluorescent co-staining
195 for Mac2/galectin-3+ cells, a marker recently identified in peripheral cell infiltrates, and IBA1
196 (Hohsfield *et al. manuscript in revision*), revealed increased monocyte/macrophage infiltration
197 within the brains of infected mice compared to sham-infected mice (**Figure 6A and B**). Mac2+
198 cells enter the CNS parenchyma from different anatomic areas including the ventricles,
199 leptomeninges and vasculature (**Figure 6C and D**) when compared to uninfected control mice
200 (**Figure 6E**).
201

bioRxiv preprint doi: https://doi.org/10.1101/2021.11.15.468761; this version posted November 17, 2021. The copyright holder for this preprint (which was not certified by peer review) is the author/funder, who has granted bioRxiv a license to display the preprint in perpetuity. It is made available under aCC-BY-NC-ND 4.0 International license.

202 **Microglia ablation does not affect disease or control of viral replication in the CNS.**
203 Previous studies have implicated the importance of microglia in aiding in control of
204 neuroadapted murine beta-coronaviruses by enhancing anti-viral T cell responses through
205 augmenting antigen presentation (11-13). Notably, microglia are dependent on signaling through
206 the colony stimulating factor 1 receptor (CSF1R) for their survival and can be effectively
207 eliminated with CSF1R inhibitors that cross the blood brain barrier [14]. K18-hACE2 mice were
208 fed pre-formulated chow containing either the CSF1R inhibitor PLX5622 (1,200 ppm) [15] or
209 control chow 7 days prior to intranasal infection with $5x10^4$ PFUs of SARS-CoV-2, and
210 remained on drug for the duration of the experiment [6]. No notable differences were detected in
211 weight loss between experimental groups (**Figure 7A**). SARS-CoV-2-infected mice treated with
212 either PLX5622 or control chow were sacrificed at day 7 p.i., and viral mRNA levels in lungs
213 and brains were determined. As shown in **Figure 7B**, we detected no significant differences in
214 the Spike mRNA transcripts in either the lung or the brain between experimental groups.
215 Quantification of Iba1-positive cells revealed a >95% reduction ($p<0.01$) in microglia in
216 PLX5622-treated mice compared to control mice. Overall, PLX5622-mediated ablation of
217 microglia resulted in a dramatic reduction in expression of proinflammatory cytokine/chemokine
218 genes within the brains of SARS-CoV-2 infected mice when compared to infected mice fed
219 control chow (**Figure 7D**). By day 7 p.i., SARS-CoV-2 infection resulted in increased expression
220 of proinflammatory cytokines and chemokines in mice treated with control chow. The highest
221 transcript levels were for the T cell chemoattractants CXCL9 and CXCL10;
222 monocyte/macrophage chemoattractants, CCL2 and CCL5; and TNF-α (**Figure 7D**). Transcripts
223 encoding the neutrophil chemoattractant CXCL1, and B cell chemoattractant CCL19 were also
224 increased, as well as IFN-λ type 3 and IL-10 when compared to uninfected controls (**Figure 7D**).

bioRxiv preprint doi: https://doi.org/10.1101/2021.11.15.468761; this version posted November 17, 2021. The copyright holder for this preprint (which was not certified by peer review) is the author/funder, who has granted bioRxiv a license to display the preprint in perpetuity. It is made available under aCC-BY-NC-ND 4.0 International license.

225 Depletion of microglia resulted in a marked reduced expression of the majority
226 chemokine/cytokines transcripts. While not significant, there was a marked reduction in
227 Mac2/galactin3+ cells in PLX5622-treated mice when compared to control chow and this
228 correlated with reduced expression of monocyte/macrophage chemoattractant chemokines CCL2
229 and CCL5 (**Figure 7E**) that have previously been shown to attract these cells into the CNS of
230 mice infected with a neurotropic mouse coronavirus [16-21].
231

bioRxiv preprint doi: https://doi.org/10.1101/2021.11.15.468761; this version posted November 17, 2021. The copyright holder for this preprint (which was not certified by peer review) is the author/funder, who has granted bioRxiv a license to display the preprint in perpetuity. It is made available under aCC-BY-NC-ND 4.0 International license.

232 **Discussion**

233 In the face of the ongoing COVID-19 pandemic, it is imperative to develop pre-clinical
234 animal models of COVID-19 that capture consistent and reproducible clinical and histologic
235 readouts of many disease-associated symptoms following experimental infection with SARS-
236 CoV-2 [1]. For both SARS-CoV-2 and SARS-CoV-1, the surface-bound viral spike glycoprotein
237 uses the cellular surface receptor protein, ACE2, to bind and enter cells. However, mouse ACE2
238 does not efficiently bind the spike glycoprotein of either SARS-CoV-1 or SARS-CoV-2,
239 rendering wildtype mice not useful in the study of SARS or COVID-19 pathogenesis,
240 respectively, due to an inefficient ability to infect and replicate in host cells. Human ACE2
241 (hACE2) transgenic mouse models have provided important insights into the pathogenesis of
242 COVID-19 in terms of evaluating the efficacy and duration of immune responses elicited in
243 response to infection as well as testing vaccines, anti-viral drugs and monoclonal antibody
244 therapies to restrict viral replication and limit disease severity [8].

245 Intranasal inoculation of K18-hACE2 mice with SARS-CoV-2 resulted in weight loss
246 along with viral infection and replication within the lungs that was associated with a robust
247 inflammatory response. These findings are consistent with other reports that demonstrated the
248 presence of neutrophils, monocytes/macrophages and T cells within the lungs of SARS-CoV-2-
249 infected K18-hACE2 mice [8, 11]. In response to infection, expression of proinflammatory
250 cytokines/chemokines was increased and correlated with the presence of inflammatory cells. We
251 detected inflammatory CD8+ T cells in the lungs of infected mice and these cells are presumably
252 responding to the T cell chemoattractant CXCL10. Our lab has previously shown that induction
253 of CXCL10 expression following experimental infection of mice with a neuroadapted strain of
254 murine coronavirus is critical in host defense and acts by attracting virus-specific T cells into the

bioRxiv preprint doi: https://doi.org/10.1101/2021.11.15.468761; this version posted November 17, 2021. The copyright holder for this preprint (which was not certified by peer review) is the author/funder, who has granted bioRxiv a license to display the preprint in perpetuity. It is made available under aCC-BY-NC-ND 4.0 International license.

255 CNS [22-24]. Similarly, inflammatory monocyte/macrophages are likely recruited in response to
256 expression of CCL2 as this has been shown to attract these cells following murine coronavirus
257 infection of mice [16-19]. The increased expression of transcripts encoding CXCR2 most likely
258 reflects the presence of inflammatory neutrophils [25]. Therapeutic targeting of these
259 chemokines may therefore alter immune cell trafficking into the lungs of infected mice and
260 alleviate the severity of lung pathology. How blocking chemokine signaling would affect SARS-
261 CoV-2-induced lung pathology in COVID-19 patients is currently under investigation.

262 Clinical reports of COVID-19 patients cite a dysregulated immune response characterized
263 by elevated chemokine expression as key in the development of pathogenesis [26, 27]. Similar to
264 our findings using the K18-hACE2 model, these reports have found upregulation of CCL2
265 (MCP1), CXCL8 (IL-8), and CXCL10 (IP10) to correlate with severity of disease and have
266 suggested evaluation of these as biomarkers for disease and as targets for therapeutic
267 intervention [28-30]. Leronlimab, a CCR5-blocking antibody, is currently in phase 2 clinical
268 trials in the U.S. for treatment of mild, moderate, and severe COVID-19 (NCT04343651,
269 NCT04347239). In addition, limiting neutrophil infiltration into the lungs of COVID-19 patients
270 may help prevent disease progression and outcome. With this in mind, the monoclonal antibody
271 BMS-986253 that blocks CXCL8 as well as Reparixin, an oral inhibitor of CXCR1/2, are both
272 currently undergoing clinical trials in the U.S. for reducing the severity of COVID-19-related
273 pneumonia by reducing neutrophil accumulation within the lungs of infected patients
274 (NCT04878055, NCT04347226). A clinical trial was recently completed using measurement of
275 CXCL10 in a Clinical Decision Support Protocol in COVID-19 patients (NCT04389645) that
276 positively correlated CXCL10 levels with mortality suggesting that targeting CXCL10 signaling
277 may also be beneficial in managing disease severity [31].

bioRxiv preprint doi: https://doi.org/10.1101/2021.11.15.468761; this version posted November 17, 2021. The copyright holder for this preprint (which was not certified by peer review) is the author/funder, who has granted bioRxiv a license to display the preprint in perpetuity. It is made available under aCC-BY-NC-ND 4.0 International license.

278 Examination of brains of SARS-CoV-2-infected K18-hACE2 mice, as well as brains
279 from other hACE2 transgenic mice, has revealed that virus is able to infect, replicate and spread
280 within the parenchyma and this is considered important in contributing to mortality [2, 5, 8, 9].
281 Virus can be detected in different anatomic regions of the brain and is accompanied by cell death
282 [5] and these observations are consistent with early studies examining SARS-CoV-1 infection of
283 K18-hACE2 mice [7]. Our results indicate that neurons are primary targets for SARS-CoV-2
284 infection within the brains of K18-hACE2 mice which is consistent with other studies [10, 32,
285 33]. Furthermore, human iPSC-derived neurons were susceptible to SARS-CoV-2 infection and
286 virus was able to replicate in these cells. The detection of viral antigen within dendrites
287 extending from the cell body suggests this may offer a unique mechanism of viral replication and
288 spread in neurons and this is further emphasized by the absence of cell death and/or syncytia
289 formation. RNA sequencing of infected neurons revealed that expression of most inflammatory
290 and anti-viral response genes were reduced in SARS-CoV-2-infected neurons, consistent with a
291 previously published study highlighting the muted immune response in neurons infected with
292 SARS-CoV-2 as compared to Zika virus [2]. However, IPA analysis determined that despite the
293 lack of induced immune and inflammatory response in infected neurons, there was a significant
294 overrepresentation of pathways associated with eIF2, oxidative phosphorylation, regulation of
295 eIF4 and mTOR signaling. eIF2, which mediates initiation of eukaryotic translation by binding
296 Met-tRNA$_i^{Met}$ to the ribosomal subunit, can be activated via phosphorylation by various kinases,
297 including protein kinase-RNA-dependent (PKR), PKR-like endoplasmic reticulum kinase
298 (PERK), and heme regulated inhibitor (HRI) [34]. Upregulation of eIF2 phosphorylation by
299 these can occur in response to various types of stressors including viral infection, ER stress, or
300 oxidative stress, respectively [34]. Upregulation of eIF4, which mediates recruitment of

bioRxiv preprint doi: https://doi.org/10.1101/2021.11.15.468761; this version posted November 17, 2021. The copyright holder for this preprint (which was not certified by peer review) is the author/funder, who has granted bioRxiv a license to display the preprint in perpetuity. It is made available under aCC-BY-NC-ND 4.0 International license.

301 ribosomes to mRNA for translation, alongside overactivation of mTOR signaling, which
302 modulates eIF4 activity, suggests infection of neurons with SARS-CoV-2 induces increased
303 cellular activity and protein production even in the absence of inflammatory and anti-viral gene
304 induction [35]. Whether this increase in protein production pathways corresponds to viral
305 hijacking of cellular machinery for viral reproduction or if it corresponds to other induced
306 mechanisms of neuronal stress/survival response remains to be determined.

307 Resident cells of the CNS are important in host defense following viral infection through
308 either secretion of anti-viral cytokines like type I interferon (IFN-I) and pro-inflammatory
309 cytokines/chemokines, and presentation of antigen to infiltration of antigen-sensitized T cells.
310 We found the transcripts encoding the T cell chemoattractant chemokines including CXCL9 and
311 CXCL10 were expressed along with monocyte/macrophage chemokines CCL2 and CCL5 and
312 CXCL1 which attracts neutrophils. In addition, transcripts specific for the B cell chemoattractant
313 CCL19 were also detected. The chemokine elicited in response to CNS infection of K18-hACE2
314 by SARS-CoV-2 infection is remarkably similar to the chemokine response following CNS
315 infection of mice with the neuroadapted strains of murine coronaviruses [36, 37]. This is
316 interesting in that murine coronavirus are primarily tropic for glial cells e.g. astrocytes, microglia
317 and oligodendrocytes with relative sparing of neurons while neurons appear to be exclusively
318 targeted by SARS-CoV-2. These findings argue that expression of chemokines following
319 coronavirus infection of the CNS may not be influenced by the cellular target of infection and
320 this may reflect a localized response to expression of interferons (IFN) expressed in response to
321 viral infection. With this in mind, we did detect IFNλ3 transcripts within the brains of SARS-
322 CoV-2 infected mice yet IFNβ1 transcripts was noticeably reduced. The inflammatory response
323 consisted primarily of monocytes/macrophages as determined by immunofluorescent staining for

bioRxiv preprint doi: https://doi.org/10.1101/2021.11.15.468761; this version posted November 17, 2021. The copyright holder for this preprint (which was not certified by peer review) is the author/funder, who has granted bioRxiv a license to display the preprint in perpetuity. It is made available under aCC-BY-NC-ND 4.0 International license.

324 Mac2 and these cells are most likely migrating into the CNS in response to CCL2 and CCL5
325 expression [18-21]. We did not detect a robust T cell response and this was surprising given the
326 expression levels of CXCL9 and CXCL10 transcripts. Whether this simply reflected that T cells
327 had yet to migrate into the brains of infected mice at the time of sacrifice or if efficient
328 translation of these transcripts is compromised is not known at this time.

329 Microglia are now recognized to be important in host defense in response to viral
330 infection of the CNS [38-42]. Targeted depletion of microglia via CSF1R inhibition leads to
331 increased mortality in mice infected with West Nile Virus (WNV) and is associated with
332 diminished activation of antigen presenting cells (APCs) and limited reactivation of virus-
333 specific T cells that leads to reduced viral clearance [39, 41]. Similar findings have been reported
334 for other neurotropic viruses including Japanese encephalitis virus (JEV) [41] and Theiler's
335 murine encephalomyelitis virus (TMEV) [40, 42]. Moreover, microglia have also been shown to
336 enhance host defense following CNS infection by the neurotropic JHM strain of mouse hepatitis
337 virus (JHMV, a murine coronavirus) and this was related to inefficient T cell-mediated control of
338 viral replication [38, 43]. Additionally, the absence of microglia also results in an increase in the
339 severity of demyelination, accompanied by a decrease in remyelination [43, 44]. In response to
340 SARS-CoV-2 CNS infection, we did detect microgliosis indicating these cells are responding to
341 infection and may be involved in host defense. Ablation of microglia via PLX5622
342 administration did not affect clinical disease nor viral burden within the brain indicating these
343 cells are dispensable in terms of controlling SARS-CoV-2 replication within the brain in the
344 K18-hACE2 model. There was a marked reduction in expression of proinflammatory
345 cytokines/chemokines including monocyte/macrophage chemoattractants CCL2 and CCL5 and
346 this corresponded with an overall reduction in numbers of these cells in the brains of PLX5622-

bioRxiv preprint doi: https://doi.org/10.1101/2021.11.15.468761; this version posted November 17, 2021. The copyright holder for this preprint (which was not certified by peer review) is the author/funder, who has granted bioRxiv a license to display the preprint in perpetuity. It is made available under aCC-BY-NC-ND 4.0 International license.

347 treated mice. These findings support the notion that microglia do contribute to the
348 neuroinflammatory response, in part, through influencing expression of chemokines/cytokines in
349 response to SARS-CoV-2 infection of the CNS of K18-hACE2 mice.

350 Very early in the COVID-19 pandemic, it became apparent that an abundant number of
351 patients exhibited a variety of neurologic conditions that ranged in severity. Although numerous
352 neurological symptoms have been associated with COVID-19, the most common neurologic
353 symptoms include anosmia/dysgeusia, delirium, encephalopathy, and stroke [45-47]. The
354 overwhelming evidence indicates that SARS-CoV-2 is not readily detected within the CNS by
355 either PCR and/or immunohistochemical staining [2, 48] suggesting that neurologic
356 complications associated with COVID-19 patients may occur through alternative mechanisms,
357 including the potential development of autoreactive antibodies specific for neural antigens [49].
358 COVID-19 patients have anti-SARS-CoV-2 IgG antibodies in the cerebral spinal fluid (CSF) that
359 recognized target epitopes that different from serum antibodies. Moreover, a portion of COVID-
360 19 patients exhibited CSF antibodies that targeted self-antigens, arguing for the possibility that
361 neurologic disease may be associated with CNS autoimmunity [49]. Nonetheless, neurons and
362 cells of the vasculature have been shown to be targets of infection [50-54]. Despite increasing
363 evidence indicating extensive SARS-CoV-2 infection of the CNS does not occur, autopsy
364 findings indicate the presence of microglia nodules, astrocyte activation and CD8+ T cell
365 infiltration in the brain, providing evidence for immune responses occurring within the CNS of
366 infected patients [3, 55, 56]. Related to this, a recent study indicated microglia nodules
367 interacting with inflammatory CD8+ T cells within distinct anatomical regions of the brains of
368 COVID-19 patients and this correlated with alerted systemic inflammation [57]. It is
369 incontrovertible that transgenic hACE2 models, particularly the K18-hACE2 model, have

bioRxiv preprint doi: https://doi.org/10.1101/2021.11.15.468761; this version posted November 17, 2021. The copyright holder for this preprint (which was not certified by peer review) is the author/funder, who has granted bioRxiv a license to display the preprint in perpetuity. It is made available under aCC-BY-NC-ND 4.0 International license.

370 provided a better understanding of the pathogenesis of COVID-19 yet the one notable and
371 consistent drawback of many of these models is the ability of virus to infect, efficiently replicate,
372 and spread within the parenchyma, which contributes to increased mortality. These findings
373 emphasize the importance of working with animal models in which SARS-CoV-2 entry into the
374 CNS is more consistent with what has been observed in COVID-19 patients.
375
376

bioRxiv preprint doi: https://doi.org/10.1101/2021.11.15.468761; this version posted November 17, 2021. The copyright holder for this preprint (which was not certified by peer review) is the author/funder, who has granted bioRxiv a license to display the preprint in perpetuity. It is made available under aCC-BY-NC-ND 4.0 International license.

377 **Materials and Methods**

378 **Mice and viral infection:** All experiments were performed in accordance with animal protocols
379 approved by the University of California, Irvine Institutional Animal Care and Use Committee.
380 8-16 week-old heterozygous K18-hACE2 C57BL/6 [strain: B6.Cg-Tg(K18-ACE2)2Prlmn/J]
381 mice were obtained from Jackson Laboratory. Animals were housed by sex in single use
382 disposable plastic cages and provided ad-libitum water. SARS-CoV-2 isolate USA-WA1/2020
383 was obtained from BEI. Mice were inoculated with between 10^4-10^5 PFU of SARS-CoV-2 in
384 10µL of DMEM or sham inoculated. Inoculations were performed under deep anesthesia through
385 an intraperitoneal injection of a mixture of ketamine and xylazine. Infected and uninfected mice
386 were examined and weighed daily. Animals were euthanized early if they reached pre-
387 determined euthanasia criteria.
388

389 **iPSC-neuronal differentiation:** iPSC line iCS83iCTR33n1 was previously derived,
390 characterized [58] and maintained as described at 37°C, 5% CO_2 - on hESC Matrigel® (Fisher
391 Scientific cat#08774552) with daily feeding of mTeSR1™ (Stem Cell Technologies cat#85850)
392 [59]. Neuronal differentiation was performed using the protocol as described [59] with a
393 modification that the cells were frozen at the neural progenitor stage at day 8 in CryoStor CS10
394 (Stem Cell Technologies #07931). Cells were thawed into LIA medium (ADF supplemented
395 with 2mM Glutamax, 2% B27 without vitamin A, 0.2µM LDN 193189 and 1.5µM IWR1
396 20ng/mL Activin A (Peprotech #120-14E)) containing 10µM Y-27632 dihydrochloride for the
397 first day post-thaw for further neural differentiation and subsequent daily feeds with LIA without
398 Y-27632 dihydrochloride. Differentiated neurons were plated at $1x10^6$ cells per well in 6-well

bioRxiv preprint doi: https://doi.org/10.1101/2021.11.15.468761; this version posted November 17, 2021. The copyright holder for this preprint (which was not certified by peer review) is the author/funder, who has granted bioRxiv a license to display the preprint in perpetuity. It is made available under aCC-BY-NC-ND 4.0 International license.

399 plate format or at 8x10^{4}cells per chamberslide well for imaging. Cells were infected with either
400 pseudovirus or SARS-CoV-2 at d46-50 after start of differentiation.
401
402 **SARS-CoV-2 infection of iPSC-derived neurons:** SARS-CoV-2 isolate USA-WA1/2020 was
403 obtained from BEI. Media was removed from cells and replaced with virus-containing media (or
404 non-virus media for mock-infection wells) at 500µL per well of a 6-well plate or 200µL per
405 chamberslide well for 1hr adsorption at 37ºC, 5% CO_2, for infection of cells at MOI = 0.1.
406 Culture plates and chamber slides were gently rocked every 15min to ensure even distribution of
407 infection media. Following 1hr adsorption, non-virus containing media was added to all cells for
408 final volume of 2mL per well of a 6-well plate or 700µL per chamberslide well and were allowed
409 to incubate with virus for 24 or 48h and then fixed with 4% PFA for subsequent
410 immunocytochemical staining. Cells in 6-well plates were allowed to incubate with virus for 24,
411 48, or 72h; supernatants were then collected, and cells harvested using 700µL of cold TRIzol
412 Reagent (Ambion, 15596018) for subsequent qPCR analysis.
413
414 **PLX5622 treatment:** Rodent chow (AIN-76A) formulated with CSF1R inhibitor-PLX5622 at a
415 dose of 1,200 ppm was provided by Plexxikon, Inc (Berkeley, CA). Mice were fed either
416 PLX5622 chow or control chow 7 days prior to viral infection, and chow was continued until
417 mice were sacrificed at defined time points post-infection.
418
419 **RNA extraction:** All RNA from VSV experiments with iPSC neurons, astrocytes, and microglia
420 was extracted via the RNeasy Mini Kit (Qiagen, 74106) using the “Purification of Total RNA
421 from Animal Cells using Spin Technology” protocol. Homogenization was performed using

bioRxiv preprint doi: https://doi.org/10.1101/2021.11.15.468761; this version posted November 17, 2021. The copyright holder for this preprint (which was not certified by peer review) is the author/funder, who has granted bioRxiv a license to display the preprint in perpetuity. It is made available under aCC-BY-NC-ND 4.0 International license.

422 QIAshredder spin columns (Qiagen, 79656). RNA from SARS-CoV-2 infected neurons was
423 extracted via the RNeasy Mini Kit using the "Purification of Total RNA, Including Small RNAs,
424 from Animal Cells" protocol. TRIzol was substituted for QIAzol, and Buffer RW1 was
425 substituted for Buffer RWT. Homogenization was performed using QIAshredder spin columns.
426 All RNA from mouse tissues was extracted via the RNeasy Mini Kit using the "Purification of
427 Total RNA, Including Small RNAs, from Animal Tissues" protocol. TRIzol was substituted for
428 QIAzol, and Buffer RW1 was substituted for Buffer RWT. Homogenization was performed
429 using the Bead Ruptor 12 (Omni International) and 1.4 mm ceramic beads (Omni International,
430 19-627). For brain tissue, the machine was set to 2 cycles at 2.25m/s for 15 seconds with a 1
431 second pause between cycles. For lungs, the machine was set to 2 cycles at 2.4m/s for 20 seconds
432 with a 1 second pause between cycles.
433
434 **cDNA synthesis:** All cDNA was made by following the "First Strand cDNA Synthesis" standard
435 protocol provided by New England Biolabs with their AMV Reverse Transcriptase (New
436 England Biolabs, M0277L). Random hexamers (Invitrogen, N8080127) were used for the
437 reactions. RNase inhibitors were not used in the cDNA synthesis.
438
439 **Gene expression analysis via quantitative PCR:** All qPCRs were performed using the Bio-Rad
440 iQ5 and iTaq™ Universal SYBR® Green Supermix (Bio-Rad, 1725120). The standard protocol
441 by Bio-Rad for iTaq™ Universal SYBR® Green Supermix was used unless otherwise stated.
442 Reactions were 10μL, and the machine was set to run for 1 cycle (95°C for 3 minutes), followed
443 by 40 cycles (95°C for 10 seconds, then 55°C for 30 seconds). The following primer sequences
444 were used:

bioRxiv preprint doi: https://doi.org/10.1101/2021.11.15.468761; this version posted November 17, 2021. The copyright holder for this preprint (which was not certified by peer review) is the author/funder, who has granted bioRxiv a license to display the preprint in perpetuity. It is made available under aCC-BY-NC-ND 4.0 International license.

Gene Target	**Forward Primer**	**Reverse Primer**
Mouse GAPDH	AACTTTGGCATTGTGGAAGG	GGATGCAGGGATGATGTTCT
Human GAPDH	CAGCCTCAAGATCATCAGCA	TGTGGTCATGAGTCCTTCCA
SARS-CoV-2 Spike	TAGTGCGTGATCTCCCTCAG	CCAGCTGTCCAACCTGAAGA

445

446 For the brain cytokine and chemokine qPCR, Qiagen's custom qPCR arrays were employed,
447 following the protocol, "Real-Time PCR for RT^2 Profiler PCR Arrays Formats A, C, D, E, F, G."
448 The plates were pre-aliquoted with primers for the following murine genes: Glyceraldehyde-3-
449 phosphate dehydrogenase (GAPDH), beta actin, chemokine ligand 10 (CXCL10), chemokine
450 ligand 9 (CXCL9), chemokine ligand 2 (CCL2), chemokine ligand 5 (CCL5), interferon gamma
451 (IFN-γ), interferon beta-1 (IFN-B1), tumor necrosis factor (TNF-α), interleukin 10 (IL10),
452 chemokine ligand 1 (CXCL1), interleukin 28B (IFN-L3), chemokine ligand 19 (CCL19).
453 Reactions were 25µL (1µL cDNA, 11.5 µL UltraPure Distilled Water (Invitrogen, 10977-015),
454 12.5 µL iTaq™ Universal SYBR® Green Supermix). The machine was set to run for 1 cycle
455 (95°C for 10 minutes), followed by 40 cycles (95°C for 15 seconds, then 60°C for 1 minute).
456 Ct values for each sample were normalized to an internal control (GAPDH), yielding the dCt
457 values. dCt values of infected or PLX-treated samples were compared to appropriate control
458 samples, as indicated, to produce ddCt values. The relative fold change between samples used in
459 the ddCt calculation was calculated (2^{-ddCt}).

460

bioRxiv preprint doi: https://doi.org/10.1101/2021.11.15.468761; this version posted November 17, 2021. The copyright holder for this preprint (which was not certified by peer review) is the author/funder, who has granted bioRxiv a license to display the preprint in perpetuity. It is made available under aCC-BY-NC-ND 4.0 International license.

461 **qPCR statistical analysis:** Statistical analysis was performed in Prism (GraphPad Software).
462 The Brown-Forsythe and Welch's ANOVA tests were used to compare the means between
463 groups. Dunnett's test to correct for multiple comparisons was performed when necessary.
464

465 **mRNA-Seq:** Total RNA was isolated using the Qiagen RNeasy Kit and QIAshredders for cell
466 lysis. One microgram of RNA with RNA integrity number values >9 was used for library
467 preparation using the strand-specific Illumina TruSeq mRNA protocol. Libraries were sequenced
468 on the NovaSeq 6000 platform using 100 cycles to obtain paired-end 100 reads at >30 million
469 reads per sample. For RNA-seq analysis, fastq files were trimmed using a base quality score
470 threshold of >20 and aligned to the hg38 genome with Hisat 2. Reads passing quality control
471 were used for quantification using featureCounts and analyzed with the R package DESeq2 to
472 identify DEGs. Genes passing an FDR of 10% were used for GO enrichment analysis using
473 GOrilla (27) (http://cbl-gorilla.cs.technion.ac.il/). For the heatmaps, a list of genes from
474 GO:0006955 immune response and GO:0006954 inflammatory response was used. From those
475 lists, the genes with the top 100 most variable TPM were plotted using the R package pheatmap.
476 For the 48h vs 24h IPA, the TPM of all genes in the 1_Infected_24h sample were subtracted
477 from the TPM of all genes in the 2_Infected_48h sample. The list of genes were sorted by the
478 difference and the top 400 and bottom 400 selected to use as input for IPA's core analysis.
479

480 **Histology and immunohistochemical staining:** Mice were euthanized at defined time points
481 post-infection and tissues harvested according to IACUC-approved guidelines. Tissues were
482 collected and placed in either cold TRIzol for qPCR analysis or 4% PFA for fixation and
483 subsequent histological analysis. Following fixation, the 24-48hr brains were either

bioRxiv preprint doi: https://doi.org/10.1101/2021.11.15.468761; this version posted November 17, 2021. The copyright holder for this preprint (which was not certified by peer review) is the author/funder, who has granted bioRxiv a license to display the preprint in perpetuity. It is made available under aCC-BY-NC-ND 4.0 International license.

484 cryoprotected in 30% sucrose, embedded in O.C.T. (Fisher HealthCare), and sliced via Cryostat
485 in 10μm sagittal sections. Alternatively, tissues were dehydrated and paraffin-embedded and
486 subsequently use for RNAscope or hematoxylin/eosin (H&E) in combination with luxol fast blue
487 (LFB) to assess demyelination within the brains of experimental mice. For immunohistochemical
488 staining of O.C.T.-embedded tissues, slides were rinsed with PBS to remove residual O.C.T., and
489 antigen retrieval (incubation with 10mM sodium Citrate at 95°C for 15min) was performed if
490 required for specific antigens at which point samples were incubated with 5% normal goat serum
491 and 0.1% Triton-X, followed by overnight incubation at 4 °C with primary antibodies. Several
492 primary antibodies were used, including Iba1 (1:500 Wako), GFAP (1:1000 Abcam), Mac2/
493 Galactin-3 (1:500, CL8942AP Cedarlane), CD4 (1:200 Abcam), CD8 (1:200 Abcam), MHC I
494 (1:200 Abcam), and MHC II (1:200 Abcam). On the second day, slides were treated with
495 appropriate secondary antibodies (1:1000 goat anti-rat/rabbit Invitrogen, 1:1000 goat anti-
496 chicken, Abcam) following PBS rinsing. Slides were then mounted with DAPI Fluoromount-G
497 (SouthernBiotech). High-resolution fluorescent images were obtained using a Leica TCS SPE-II
498 confocal microscope and LAS-X software. For whole brain stitches, automated slide scanning
499 was performed using a Zeiss AxioScan.Z1 equipped with a Colibri camera and Zen AxioScan
500 2.3 software. Microglial morphology was determined using the filaments module in Bitplane
501 Imaris 7.5, as described previously (Elmore, Lee, West, & Green, 2015). Cell quantities were
502 determined using the spots module in Imaris.
503
504 **RNAscope in situ hybridization of SARS-CoV-2 spike RNA:** RNA in situ hybridization was
505 performed via RNAscope 2.5 HD Red Assay Kit (Advanced Cell Diagnostics, Cat: 322350) in
506 accordance with manufacturer's instructions. Fixed tissue sections were treated with the

bioRxiv preprint doi: https://doi.org/10.1101/2021.11.15.468761; this version posted November 17, 2021. The copyright holder for this preprint (which was not certified by peer review) is the author/funder, who has granted bioRxiv a license to display the preprint in perpetuity. It is made available under aCC-BY-NC-ND 4.0 International license.

507 manufacturer's Fresh Frozen Tissue Sample Preparation Protocol, fixed in chilled 4% PFA,
508 dehydrated, and treated with H_2O_2 and Protease IV before probe hybridization. Paraffinized
509 sections were deparaffinized and treated with H_2O_2 and Protease Plus prior to hybridization.
510 Probes targeting SARS-CoV-2 spike (Cat: 848561), positive control Hs-PPIB (Cat: 313901), or
511 negative control DapB (Cat: 310043) were hybridized followed by proprietary assay signal
512 amplification and detection. Tissues were counterstained with Gill's hematoxylin. An uninfected
513 mouse was used as a negative control and stained in parallel. Tissues were visualized using an
514 Olympus BX60 microscope and imaged with a Nikon (Model #) camera.
515
516 **Immunocytochemical staining for SARS-CoV-2:** iPSC-derived neurons on glass-bottomed 4-
517 well chamberslides were gently washed with 1X PBS and fixed for 1hr with 4%
518 paraformaldehyde for removal from BSL-3 facility. Wells were subsequently washed 3 times
519 with 1X PBS, permeabilized for 15min at RT in 0.1% Triton-X in PBS and blocked for 2hrs in a
520 2% BSA-5% NDS blocking solution. Cells were incubated overnight at 4ºC in blocking solution
521 with primary antibodies anti-MAP2 (EnCor Biotech. Cat:NC0388389) and anti-SARS-CoV-2
522 nucleocapsid (Sino Bio. Cat: 40143-R019). Cells were then washed with 1X PBS and incubated
523 in blocking solution for 2hrs at RT with secondary antibodies, Alexa Fluor 594-conjugated goat
524 anti-chicken and Alexa Fluor 488-conjugated goat anti-rabbit. After staining, cells were imaged
525 for presence of SARS-CoV-2 nucleocapsid staining and quantified using the Revolve D75.
526
527

bioRxiv preprint doi: https://doi.org/10.1101/2021.11.15.468761; this version posted November 17, 2021. The copyright holder for this preprint (which was not certified by peer review) is the author/funder, who has granted bioRxiv a license to display the preprint in perpetuity. It is made available under aCC-BY-NC-ND 4.0 International license.

528 **Acknowledgements**

529 This work was supported by a COVID CRAFT grant from UC Irvine Office of Research, NIH-
530 NINDS R35 NS116835, NIH-NINDS NS041249, National Multiple Sclerosis Society grant CA-
531 1607-25040 and support from the Ray and Tye Noorda Foundation to T.E.L. L.M.T. was
532 supported by NIH-NINDS R35 NS116872 and K.N.G. was supported by NIH-NINDS
533 R01NS083801. G.M.O. was supported by Immunology Research Training Grant
534 5T32AI060573-15 and C.S-G was supported by the Hereditary Disease Foundation. The authors
535 wish to acknowledge the support of the Chao Family Comprehensive Cancer Center
536 Experimental Tissue Shared Resource supported by the National Cancer Institute of the National
537 Institutes of Health under award number P30CA062203.
538

539

bioRxiv preprint doi: https://doi.org/10.1101/2021.11.15.468761; this version posted November 17, 2021. The copyright holder for this preprint (which was not certified by peer review) is the author/funder, who has granted bioRxiv a license to display the preprint in perpetuity. It is made available under aCC-BY-NC-ND 4.0 International license.

540 **Figure Legends**
541
542 **Figure 1. SARS-CoV-2 infects human iPSC-derived neurons.** (**A**) hiPSC-derived neurons
543 were infected with SARS-CoV-2 at an MOI of 0.1, immunostained with anti-MAP2 and anti-
544 SARS-CoV-2 N, and imaged at 0, 24, and 48 hours post-infection. (**B**) Quantification of SARS-
545 CoV-2 GFP fluorescence of mock-infected and SARS-CoV-2-infected hiPSC-derived neurons.
546 (**C**) Perinuclear replication of SARS-CoV-2 in neuronal soma (arrowhead) but no viral axonal
547 (arrows) transport at 24 hours post-infection. (**D**) Perinuclear presence of SARS-CoV-2 in soma
548 (arrowhead) and axon (arrows) at 24 hours post-infection. (**E**) Heat map of genes expressed 24
549 and 48h post-infection. **(F)** Top 12 canonical pathways showing progressive changes from 24 to
550 48 h post-infection.
551
552 **Figure 2. SARS-CoV-2 infection of lungs of K18-hACE2 mice.** (**A**) Percent weight change of
553 K18-hACE2 and WT mice infected with indicated dose of SARS-CoV-2. C57BL/6 wildtype
554 (WT) mice (n=3) were infected with 1x104 PFU. K18-hACE2 mice were infected intranasally
555 with SARS-CoV-2 at either $1x10^4$ PFU (n=17), $5x10^4$ PFU (n=4), or $1x10^5$PFU (n=8). (**B**)
556 Quantitative PCR with primers for Spike mRNA on uninfected and SARS-CoV-2-infected
557 mouse lung tissue. dCt values are derived from the difference between the Ct values of Spike
558 mRNA and a housekeeping gene, GAPDH. Lower dCt values indicate increased viral mRNA.
559 (**C**) K18-hACE2 mouse lung tissue at day 7 p.i. with $5x10^4$ PFU SARS-CoV-2 showing
560 localized Spike mRNA expression as determined by RNAscope. Representative H&E images
561 from lungs of SARS-CoV-2-infected mice ($5x10^4$ PFU) showing (**D**) airway edema, vascular
562 congestion and intra-alveolar hemorrhage, (**E**) peri-bronchiolar lymphocytic cuffing, and (**F**)
563 Interstitial vascular congestion and lymphocytic infiltrates. (**G**) Quantitative PCR shows the fold
564 changes of the indicated genes in two infected mouse lungs compared to uninfected mice.
565
566 **Figure 3. CD8+ T cell infiltration into lungs of SARS-CoV-2-infected mice.** H&E staining of
567 lungs of SARS-CoV-2 infected mice at day 7 post-infection reveal inflammation (**A** and **C**)
568 associated with CD8+ T cell infiltration (**B** and **D**) as determined by immunofluorescent staining.
569 Lymph node-like structures were also detected containing CD8+ T cells (**E** and **F**). Panels *A*, *C*,
570 and *E* 10X magnification; panels *B*, *D*, and *F* 20X magnification.
571
572 **Figure 4. Widespread neuroinvasion by SARS-CoV-2 of K18 human-ACE2 mice. (A)**
573 Quantitative PCR with primers for Spike mRNA on uninfected and SARS-CoV-2-infected
574 mouse brain tissue at day 7 p.i. dCt values are derived from the difference between the Ct values
575 of Spike mRNA and the housekeeping gene, GAPDH. *In situ* hybridization for Spike viral
576 mRNA in (**B**) SARS-CoV-2-infected and (**C**) sham-infected K18-hACE2 mice. Anatomical
577 regions in which viral RNA is detected (indicated in red) are indicated: cortex (CTX), striatum
578 (STR), pallidum (PAL), thalamus (TH), hypothalamus (HY), midbrain (MB), Pons (P), and
579 medulla (MD), whereas areas that were relatively spared included the olfactory bulb (OB), white
580 matter (WM) tracts and hippocampus (HC) (**D**) Representative brain from SARS-CoV-2
581 infected brain from panel *B* stained with LFB demonstrates lack of demyelination with (**E**) high-
582 power image of myelin tract showing no inflammation or demyelination.
583
584 **Figure 5. Neurons are targets of infection within the brains of SARS-CoV-2 infected K18-**
585 **hACE2 mice.** Brains of SARS-CoV-2 infected mice at day 7 p.i. were analyzed to assess cellular

bioRxiv preprint doi: https://doi.org/10.1101/2021.11.15.468761; this version posted November 17, 2021. The copyright holder for this preprint (which was not certified by peer review) is the author/funder, who has granted bioRxiv a license to display the preprint in perpetuity. It is made available under aCC-BY-NC-ND 4.0 International license.

586 targets of infection through *in situ* hybridization using RNAscope *in situ* hybridization using
587 Spike-specific probes. (**A**) Cells within the cortex with neuron morphology were primary targets
588 of infection; (**B**) high-power image of cells boxed in panel *A* show viral RNA present within cell
589 body as well as extending down dendrites extending from the cell body. (**C**) Viral RNA was also
590 detected in olfactory bulbs at day 7 p.i. (**D**) high-power image cells boxed in panel *C* reveal
591 neurons in the mitral (open arrow) and glomerular (closed arrow) are infected by virus.
592 Representative H&E images from the brains of infected K18-hACE2 mice at day 7 p.i. depicting
593 (**E**) perivascular cuffing, (**F**) subventricular inflammation, and (**G**) leptomeningitis.
594
595 **Figure 6. SARS-CoV-2 infection of K18 human-ACE2 mice results in microgliosis and**
596 **myeloid cell infiltration.** Brains from either SARS-CoV-2 or sham-infected mice were removed
597 at day 7 p.i. to evaluate immune cell infiltration. Microglia activation and monocyte infiltration
598 were determined in sham-infected mice **(A)** and SARS-CoV2 infected mice **(B)** by staining for
599 expression of Iba1 (red) and Mac2/galectin 3 (green), respectively. Infiltration of peripheral
600 monocytes into the SARS-CoV-2 infected brain parenchyma occurs via the vasculature (**C**) as
601 well as ventricular and leptomeningeal spaces (**D**) compared to uninfected control mice (**E**).
602
603 **Figure 7 Microglia ablation does not impact control of viral replication in the CNS**. (**A**)
604 Weight loss of K18-hACE2 mice infected intranasally with $5x10^4$ PFU of SARS-CoV-2 that
605 were fed either control chow (n=4) of PLX5622-formulated chow (n=4). (**B**) Quantitative PCR
606 in the brains and lungs of infected PLX-treated and non-PLX-treated mice shows no significant
607 difference in the levels of Spike mRNA in either lung or brain tissue as a result of PLX5622
608 treatment. **(C)** Quantification of Iba1-positive cells in the somatosensory cortex shows a
609 significant (**p<0.01) depletion of microglia from PLX5622 treated mice compared to control
610 mice. (**D**) qPCR analysis of brains of experimental mice indicated a reduction in expression of
611 pro-inflammatory cytokines/chemokines in the brains of PLX5622-treated mice compared to
612 control mice. **(E)** Quantification of Mac2-positive cells in the somatosensory cortex an overall
613 trend in reduced numbers in PLX5622-treated mice compared to controls. Brains from SARS-
614 CoV-2-infected mice treated with either (**F**) control chow or (**G**) PLX5622 were stained with
615 LFB to assess demyelination or the presence of viral RNA determined by RNAscope.
616 Representative brain sections are from experimental mice at day 7 p.i.
617
618
619
620
621
622
623
624
625
626

bioRxiv preprint doi: https://doi.org/10.1101/2021.11.15.468761; this version posted November 17, 2021. The copyright holder for this preprint (which was not certified by peer review) is the author/funder, who has granted bioRxiv a license to display the preprint in perpetuity. It is made available under aCC-BY-NC-ND 4.0 International license.

627
628
629 **Literature Cited**
630

631 1. Channappanavar, R. and S. Perlman, *Age-related susceptibility to coronavirus infections:*
632 *role of impaired and dysregulated host immunity.* J Clin Invest, 2020. **130**(12): p. 6204-
633 6213.
634 2. Song, E., et al., *Neuroinvasion of SARS-CoV-2 in human and mouse brain.* J Exp Med,
635 2021. **218**(3).
636 3. Lou, J.J., et al., *Neuropathology of COVID-19 (neuro-COVID): clinicopathological*
637 *update.* Free Neuropathol, 2021. **2**.
638 4. Virhammar, J., et al., *Acute necrotizing encephalopathy with SARS-CoV-2 RNA*
639 *confirmed in cerebrospinal fluid.* Neurology, 2020. **95**(10): p. 445-449.
640 5. Pellegrini, L., et al., *SARS-CoV-2 Infects the Brain Choroid Plexus and Disrupts the*
641 *Blood-CSF Barrier in Human Brain Organoids.* Cell Stem Cell, 2020. **27**(6): p. 951-961
642 e5.
643 6. Munoz-Fontela, C., et al., *Animal models for COVID-19.* Nature, 2020. **586**(7830): p.
644 509-515.
645 7. McCray, P.B., Jr., et al., *Lethal infection of K18-hACE2 mice infected with severe acute*
646 *respiratory syndrome coronavirus.* J Virol, 2007. **81**(2): p. 813-21.
647 8. Zheng, J., et al., *COVID-19 treatments and pathogenesis including anosmia in K18-*
648 *hACE2 mice.* Nature, 2021. **589**(7843): p. 603-607.
649 9. Bao, L., et al., *The pathogenicity of SARS-CoV-2 in hACE2 transgenic mice.* Nature,
650 2020. **583**(7818): p. 830-833.
651 10. Sun, S.H., et al., *A Mouse Model of SARS-CoV-2 Infection and Pathogenesis.* Cell Host
652 Microbe, 2020. **28**(1): p. 124-133 e4.
653 11. Winkler, E.S., et al., *Publisher Correction: SARS-CoV-2 infection of human ACE2-*
654 *transgenic mice causes severe lung inflammation and impaired function.* Nat Immunol,
655 2020. **21**(11): p. 1470.
656 12. Jiang, R.D., et al., *Pathogenesis of SARS-CoV-2 in Transgenic Mice Expressing Human*
657 *Angiotensin-Converting Enzyme 2.* Cell, 2020. **182**(1): p. 50-58 e8.
658 13. Reichard, R.R., et al., *Neuropathology of COVID-19: a spectrum of vascular and acute*
659 *disseminated encephalomyelitis (ADEM)-like pathology.* Acta Neuropathol, 2020. **140**(1):
660 p. 1-6.
661 14. Elmore, M.R., et al., *Colony-stimulating factor 1 receptor signaling is necessary for*
662 *microglia viability, unmasking a microglia progenitor cell in the adult brain.* Neuron,
663 2014. **82**(2): p. 380-97.
664 15. Spangenberg, E., et al., *Sustained microglial depletion with CSF1R inhibitor impairs*
665 *parenchymal plaque development in an Alzheimer's disease model.* Nat Commun, 2019.
666 **10**(1): p. 3758.
667 16. Trujillo, J.A., E.L. Fleming, and S. Perlman, *Transgenic CCL2 expression in the central*
668 *nervous system results in a dysregulated immune response and enhanced lethality after*
669 *coronavirus infection.* J Virol, 2013. **87**(5): p. 2376-89.
670 17. Kim, T.S. and S. Perlman, *Viral expression of CCL2 is sufficient to induce demyelination*
671 *in RAG1-/- mice infected with a neurotropic coronavirus.* J Virol, 2005. **79**(11): p. 7113-
672 7120.

bioRxiv preprint doi: https://doi.org/10.1101/2021.11.15.468761; this version posted November 17, 2021. The copyright holder for this preprint (which was not certified by peer review) is the author/funder, who has granted bioRxiv a license to display the preprint in perpetuity. It is made available under aCC-BY-NC-ND 4.0 International license.

673 18. Held, K.S., et al., *Differential roles of CCL2 and CCR2 in host defense to coronavirus*
674 *infection.* Virology, 2004. **329**(2): p. 251-60.
675 19. Chen, B.P., W.A. Kuziel, and T.E. Lane, *Lack of CCR2 results in increased mortality and*
676 *impaired leukocyte activation and trafficking following infection of the central nervous*
677 *system with a neurotropic coronavirus.* J Immunol, 2001. **167**(8): p. 4585-92.
678 20. Glass, W.G., et al., *Antibody Targeting of the CC Chemokine Ligand 5 Results in*
679 *Diminished Leukocyte Infiltration into the Central Nervous System and Reduced*
680 *Neurologic Disease in a Viral Model of Multiple Sclerosis.* The Journal of Immunology,
681 2004. **172**(7): p. 4018-4025.
682 21. Glass, W.G., et al., *Reduced macrophage infiltration and demyelination in mice lacking*
683 *the chemokine receptor CCR5 following infection with a neurotropic coronavirus.*
684 Virology, 2001. **288**(1): p. 8-17.
685 22. Liu, M.T., et al., *Cutting Edge: The T Cell Chemoattractant IFN-Inducible Protein 10 Is*
686 *Essential in Host Defense Against Viral-Induced Neurologic Disease.* The Journal of
687 Immunology, 2000. **165**(5): p. 2327-2330.
688 23. Stiles, L.N., et al., *T cell antiviral effector function is not dependent on CXCL10*
689 *following murine coronavirus infection.* J Immunol, 2006. **177**(12): p. 8372-80.
690 24. Stiles, L.N., et al., *CXCL10 and trafficking of virus-specific T cells during coronavirus*
691 *demyelination.* Autoimmunity, 2009. **In Press**.
692 25. Hosking, M.P., et al., *A protective role for ELR+ chemokines during acute viral*
693 *encephalomyelitis.* PLoS Pathog, 2009. **5**(11): p. e1000648.
694 26. Lowery, S.A., A. Sariol, and S. Perlman, *Innate immune and inflammatory responses to*
695 *SARS-CoV-2: Implications for COVID-19.* Cell Host Microbe, 2021. **29**(7): p. 1052-
696 1062.
697 27. Channappanavar, R. and S. Perlman, *Pathogenic human coronavirus infections: causes*
698 *and consequences of cytokine storm and immunopathology.* Semin Immunopathol, 2017.
699 **39**(5): p. 529-539.
700 28. Alosaimi, B., et al., *Complement Anaphylatoxins and Inflammatory Cytokines as*
701 *Prognostic Markers for COVID-19 Severity and In-Hospital Mortality.* Front Immunol,
702 2021. **12**: p. 668725.
703 29. Huang, C., et al., *Clinical features of patients infected with 2019 novel coronavirus in*
704 *Wuhan, China.* Lancet, 2020. **395**(10223): p. 497-506.
705 30. Laudanski, K., et al., *Unbiased Analysis of Temporal Changes in Immune Serum Markers*
706 *in Acute COVID-19 Infection With Emphasis on Organ Failure, Anti-Viral Treatment,*
707 *and Demographic Characteristics.* Front Immunol, 2021. **12**: p. 650465.
708 31. Lev, S., et al., *Observational cohort study of IP-10's potential as a biomarker to aid in*
709 *inflammation regulation within a clinical decision support protocol for patients with*
710 *severe COVID-19.* PLoS One, 2021. **16**(1): p. e0245296.
711 32. Kumari, P., et al., *Neuroinvasion and Encephalitis Following Intranasal Inoculation of*
712 *SARS-CoV-2 in K18-hACE2 Mice.* Viruses, 2021. **13**(1).
713 33. Carossino, M., et al., *Fatal neuroinvasion of SARS-CoV-2 in K18-hACE2 mice is*
714 *partially dependent on hACE2 expression.* bioRxiv, 2021.
715 34. Schmitt, E., M. Naveau, and Y. Mechulam, *Eukaryotic and archaeal translation*
716 *initiation factor 2: a heterotrimeric tRNA carrier.* FEBS Lett, 2010. **584**(2): p. 405-12.

bioRxiv preprint doi: https://doi.org/10.1101/2021.11.15.468761; this version posted November 17, 2021. The copyright holder for this preprint (which was not certified by peer review) is the author/funder, who has granted bioRxiv a license to display the preprint in perpetuity. It is made available under aCC-BY-NC-ND 4.0 International license.

717 35. Showkat, M., M.A. Beigh, and K.I. Andrabi, *mTOR Signaling in Protein Translation*
718 *Regulation: Implications in Cancer Genesis and Therapeutic Interventions.* Mol Biol Int,
719 2014. **2014**: p. 686984.
720 36. Lane, T.E., et al., *Dynamic regulation of alpha- and beta-chemokine expression in the*
721 *central nervous system during mouse hepatitis virus-induced demyelinating disease.* J
722 Immunol, 1998. **160**(2): p. 970-8.
723 37. Syage, A.R., et al., *Single-Cell RNA Sequencing Reveals the Diversity of the*
724 *Immunological Landscape following Central Nervous System Infection by a Murine*
725 *Coronavirus.* J Virol, 2020. **94**(24).
726 38. Wheeler, D.L., et al., *Microglia are required for protection against lethal coronavirus*
727 *encephalitis in mice.* J Clin Invest, 2018. **128**(3): p. 931-943.
728 39. Funk, K.E. and R.S. Klein, *CSF1R antagonism limits local restimulation of antiviral*
729 *CD8(+) T cells during viral encephalitis.* J Neuroinflammation, 2019. **16**(1): p. 22.
730 40. Sanchez, J.M.S., et al., *Microglial cell depletion is fatal with low level picornavirus*
731 *infection of the central nervous system.* J Neurovirol, 2019. **25**(3): p. 415-421.
732 41. Seitz, S., P. Clarke, and K.L. Tyler, *Pharmacologic Depletion of Microglia Increases*
733 *Viral Load in the Brain and Enhances Mortality in Murine Models of Flavivirus-Induced*
734 *Encephalitis.* J Virol, 2018. **92**(16).
735 42. Waltl, I., et al., *Microglia have a protective role in viral encephalitis-induced seizure*
736 *development and hippocampal damage.* Brain Behav Immun, 2018. **74**: p. 186-204.
737 43. Mangale, V., et al., *Microglia influence host defense, disease, and repair following*
738 *murine coronavirus infection of the central nervous system.* Glia, 2020. **68**(11): p. 2345-
739 2360.
740 44. Sariol, A., et al., *Microglia depletion exacerbates demyelination and impairs*
741 *remyelination in a neurotropic coronavirus infection.* Proc Natl Acad Sci U S A, 2020.
742 **117**(39): p. 24464-24474.
743 45. Glatzel, M., et al., *Neuropathology associated with SARS-CoV-2 infection.* Lancet, 2021.
744 **397**(10271): p. 276.
745 46. Leven, Y. and J. Bosel, *Neurological manifestations of COVID-19 - an approach to*
746 *categories of pathology.* Neurol Res Pract, 2021. **3**(1): p. 39.
747 47. Johansson, A., et al., *Neurological manifestations of COVID-19: A comprehensive*
748 *literature review and discussion of mechanisms.* J Neuroimmunol, 2021. **358**: p. 577658.
749 48. Matschke, J., et al., *Neuropathology of patients with COVID-19 in Germany: a post-*
750 *mortem case series.* Lancet Neurol, 2020. **19**(11): p. 919-929.
751 49. Song, E., et al., *Divergent and self-reactive immune responses in the CNS of COVID-19*
752 *patients with neurological symptoms.* Cell Rep Med, 2021. **2**(5): p. 100288.
753 50. Yang, A.C., et al., *Dysregulation of brain and choroid plexus cell types in severe*
754 *COVID-19.* Nature, 2021. **595**(7868): p. 565-571.
755 51. Karuppan, M.K.M., et al., *SARS-CoV-2 Infection in the Central and Peripheral Nervous*
756 *System-Associated Morbidities and Their Potential Mechanism.* Mol Neurobiol, 2021.
757 **58**(6): p. 2465-2480.
758 52. Akhter, N., et al., *Impact of COVID-19 on the cerebrovascular system and the prevention*
759 *of RBC lysis.* Eur Rev Med Pharmacol Sci, 2020. **24**(19): p. 10267-10278.
760 53. Chia, K.X., S. Polakhare, and S.D. Bruno, *Possible affective cognitive cerebellar*
761 *syndrome in a young patient with COVID-19 CNS vasculopathy and stroke.* BMJ Case
762 Rep, 2020. **13**(10).

bioRxiv preprint doi: https://doi.org/10.1101/2021.11.15.468761; this version posted November 17, 2021. The copyright holder for this preprint (which was not certified by peer review) is the author/funder, who has granted bioRxiv a license to display the preprint in perpetuity. It is made available under aCC-BY-NC-ND 4.0 International license.

763 54. MacLean, M.A., et al., *The potential role of microvascular pathology in the neurological*
764 *manifestations of coronavirus infection.* Fluids Barriers CNS, 2020. **17**(1): p. 55.
765 55. Thakur, K.T., et al., *COVID-19 neuropathology at Columbia University Irving Medical*
766 *Center/New York Presbyterian Hospital.* Brain, 2021. **144**(9): p. 2696-2708.
767 56. Al-Dalahmah, O., et al., *Neuronophagia and microglial nodules in a SARS-CoV-2 patient*
768 *with cerebellar hemorrhage.* Acta Neuropathol Commun, 2020. **8**(1): p. 147.
769 57. Schwabenland, M., et al., *Deep spatial profiling of human COVID-19 brains reveals*
770 *neuroinflammation with distinct microanatomical microglia-T-cell interactions.*
771 Immunity, 2021. **54**(7): p. 1594-1610 e11.
772 58. Consortium, H.D.i., *Induced pluripotent stem cells from patients with Huntington's*
773 *disease show CAG-repeat-expansion-associated phenotypes.* Cell Stem Cell, 2012. **11**(2):
774 p. 264-78.
775 59. Smith-Geater, C., et al., *Aberrant Development Corrected in Adult-Onset Huntington's*
776 *Disease iPSC-Derived Neuronal Cultures via WNT Signaling Modulation.* Stem Cell
777 Reports, 2020. **14**(3): p. 406-419.
778
779
780
781
782
783
784

bioRxiv preprint doi: https://doi.org/10.1101/2021.11.15.468761; this version posted November 17, 2021. The copyright holder for this preprint (which was not certified by peer review) is the author/funder, who has granted bioRxiv a license to display the preprint in perpetuity. It is made available under aCC-BY-NC-ND 4.0 International license.

A

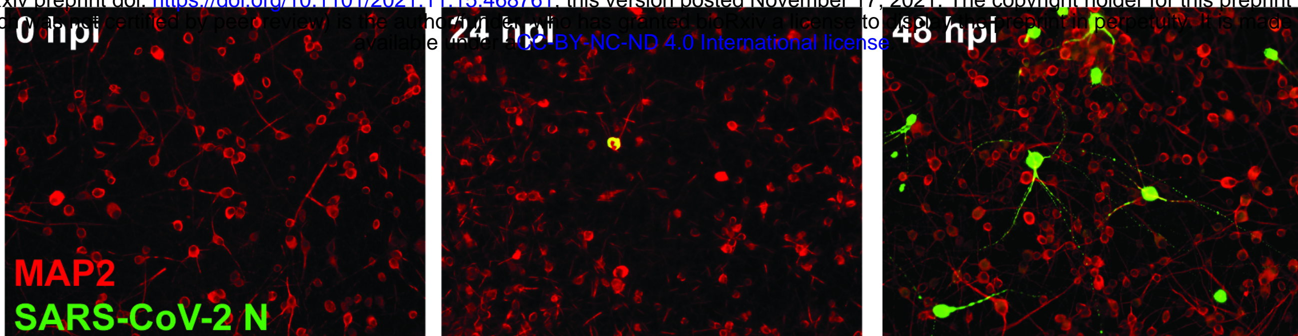

B

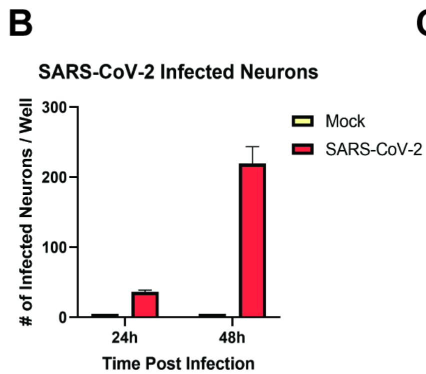

C

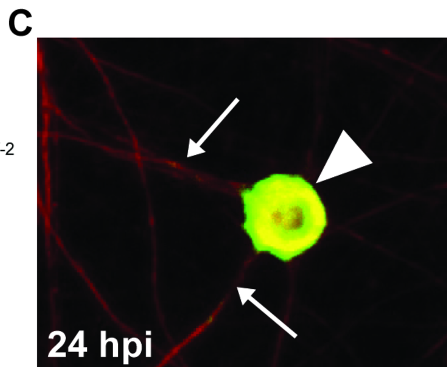

D

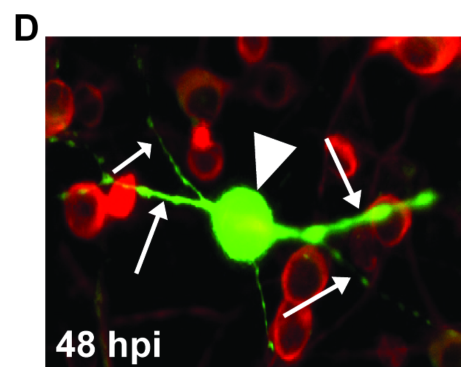

E

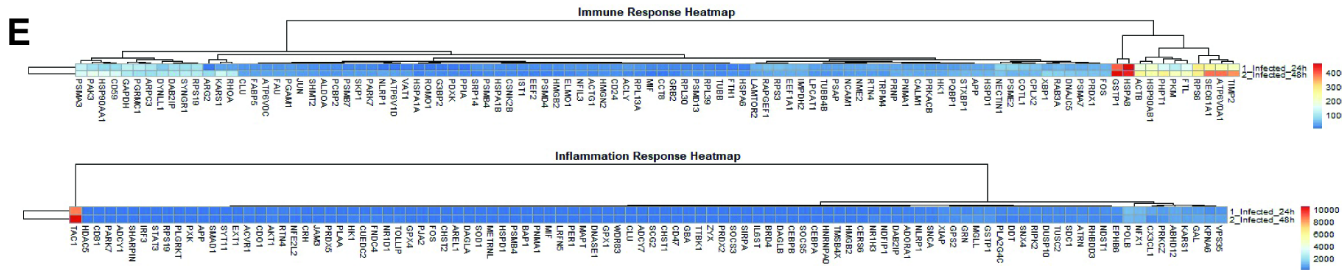

F

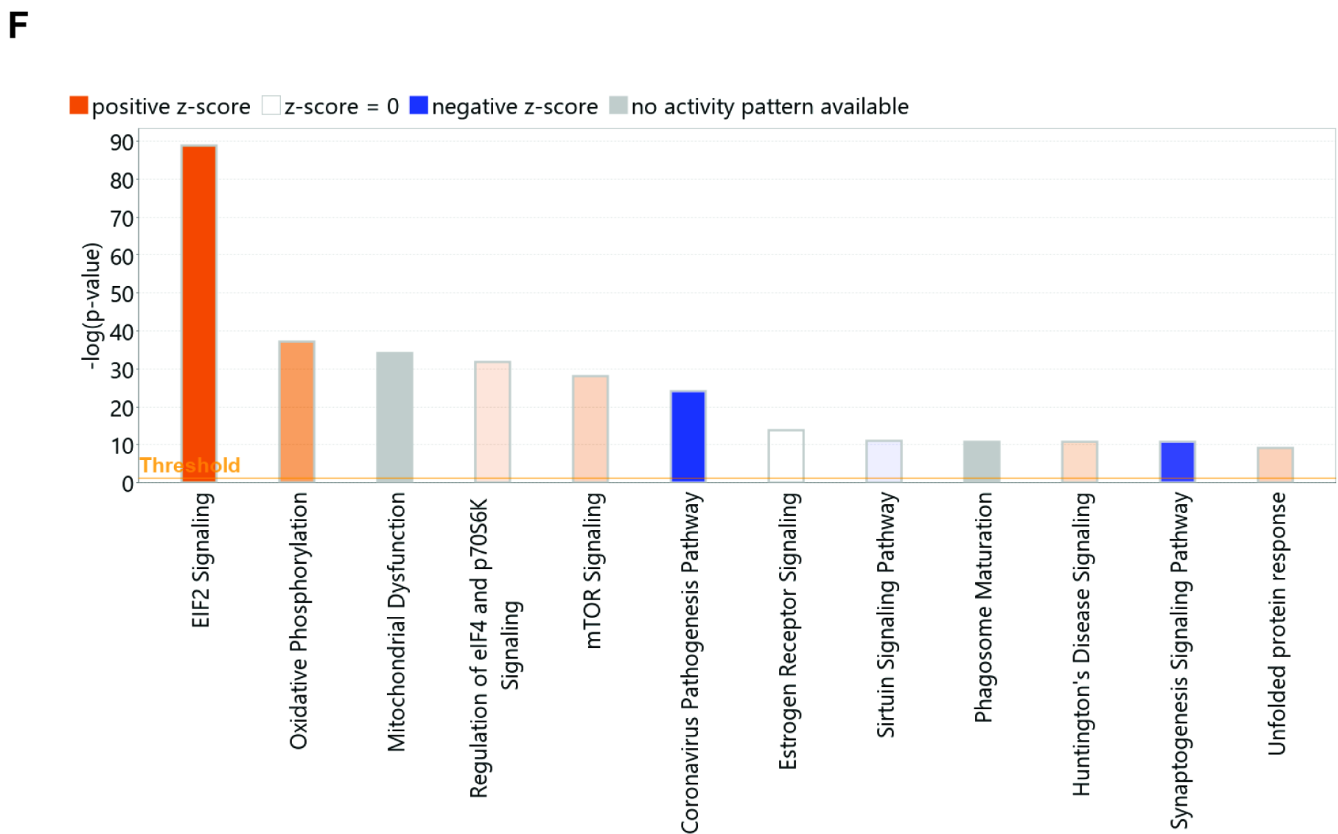

bioRxiv preprint doi: https://doi.org/10.1101/2021.11.15.468761; this version posted November 17, 2021. The copyright holder for this preprint (which was not certified by peer review) is the author/funder, who has granted bioRxiv a license to display the preprint in perpetuity. It is made available under aCC-BY-NC-ND 4.0 International license.

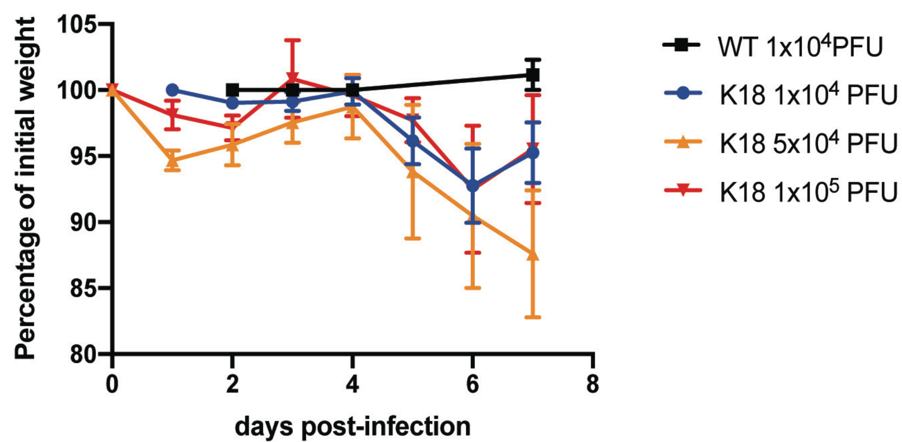

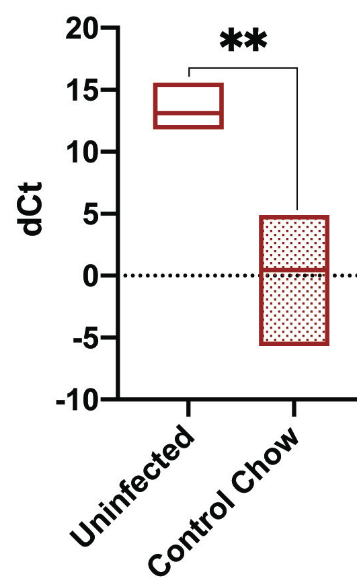

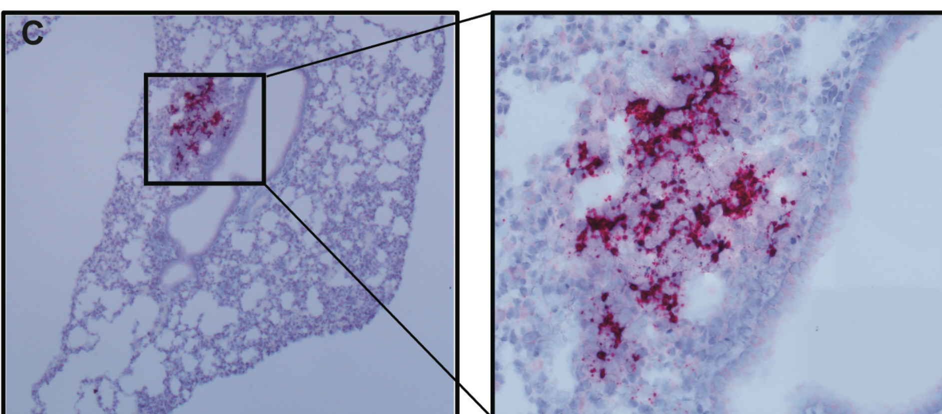

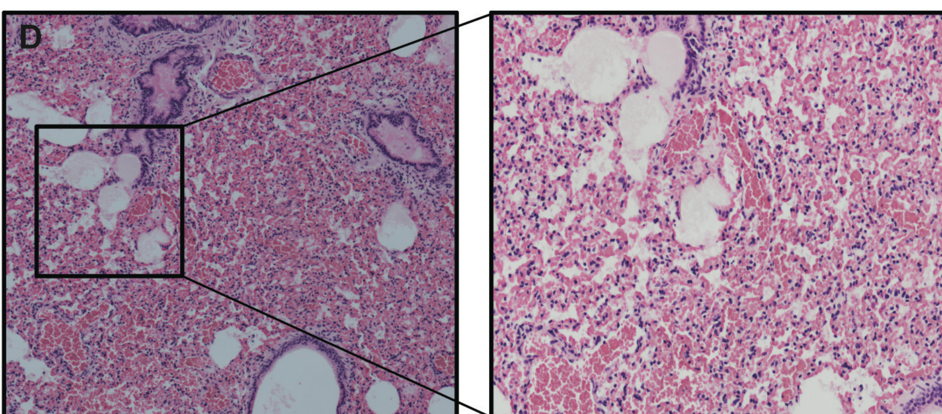

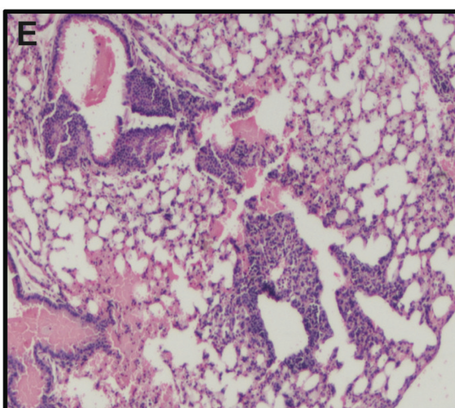

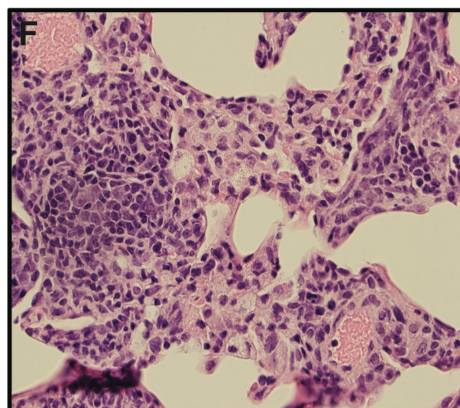

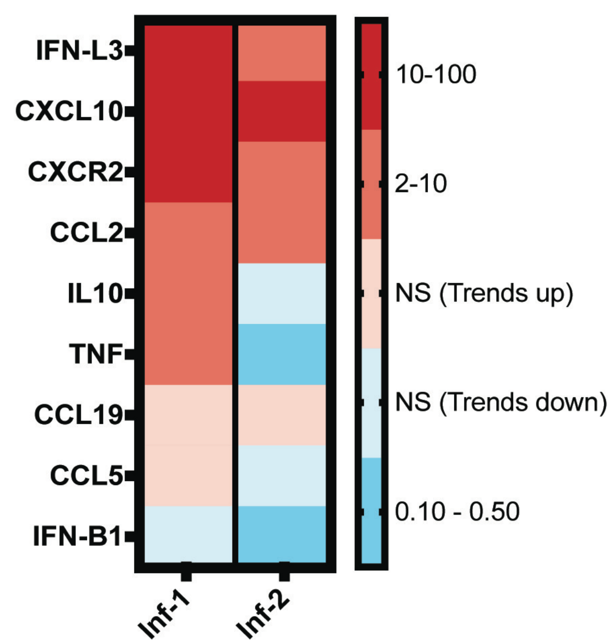

bioRxiv preprint doi: https://doi.org/10.1101/2021.11.15.468761; this version posted November 17, 2021. The copyright holder for this preprint (which was not certified by peer review) is the author/funder, who has granted bioRxiv a license to display the preprint in perpetuity. It is made available under aCC-BY-NC-ND 4.0 International license.

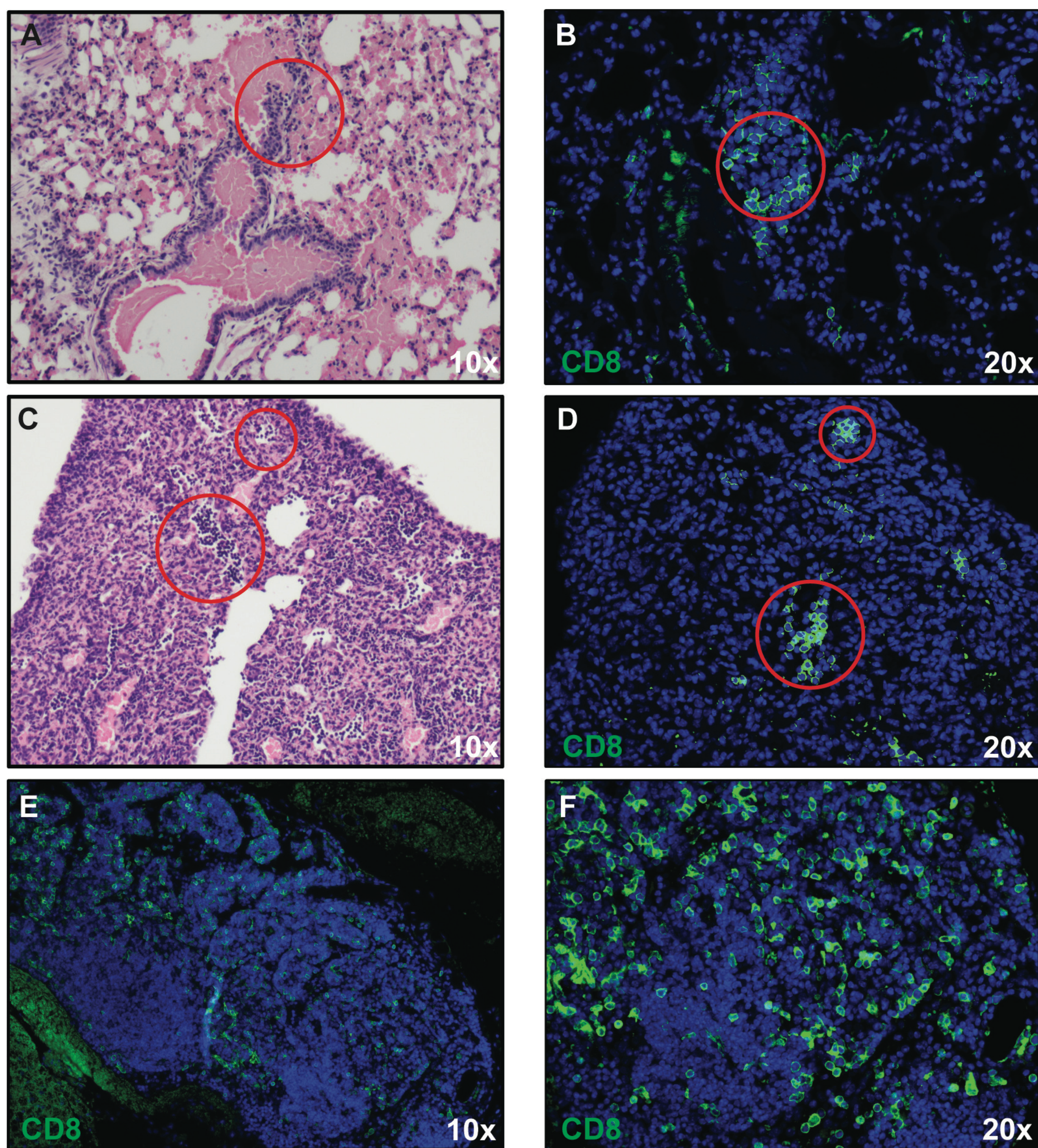

bioRxiv preprint doi: https://doi.org/10.1101/2021.11.15.468761; this version posted November 17, 2021. The copyright holder for this preprint (which was not certified by peer review) is the author/funder, who has granted bioRxiv a license to display the preprint in perpetuity. It is made available under aCC-BY-NC-ND 4.0 International license.

A

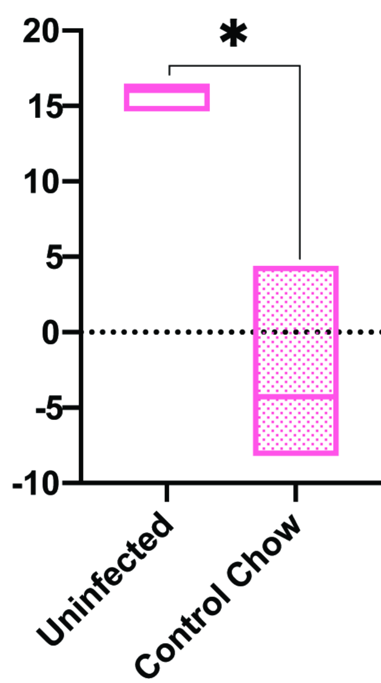

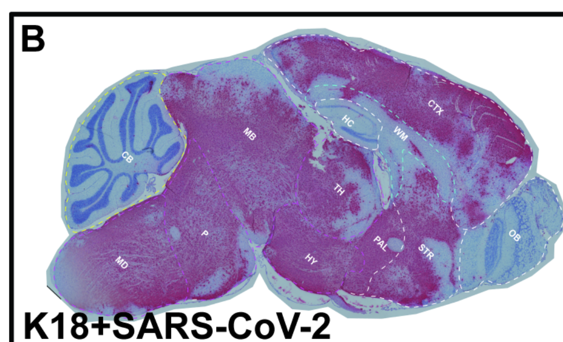

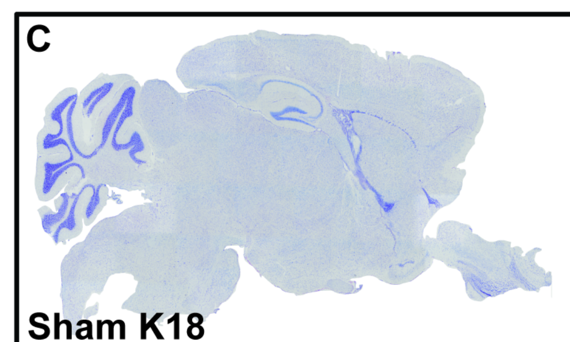

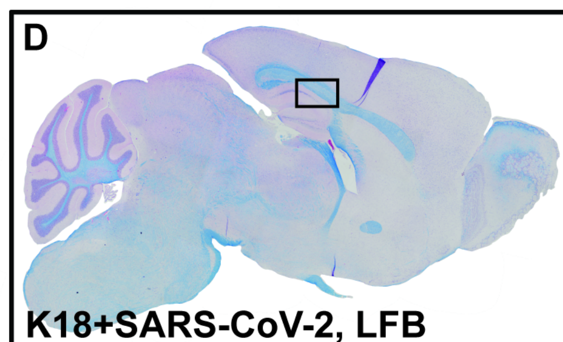

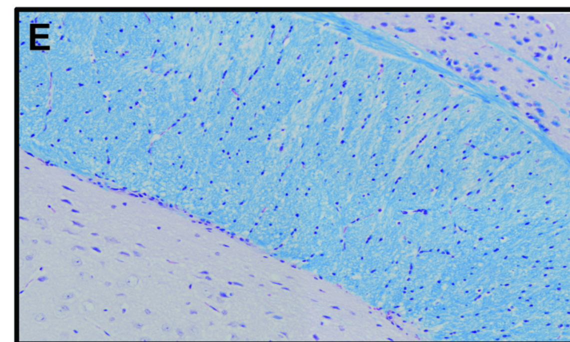

bioRxiv preprint doi: https://doi.org/10.1101/2021.11.15.468761; this version posted November 17, 2021. The copyright holder for this preprint (which was not certified by peer review) is the author/funder, who has granted bioRxiv a license to display the preprint in perpetuity. It is made available under aCC-BY-NC-ND 4.0 International license.

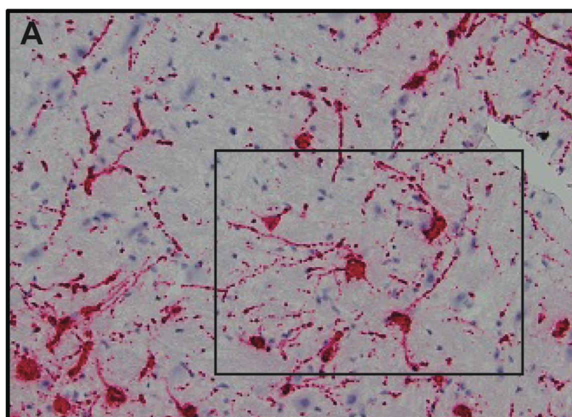

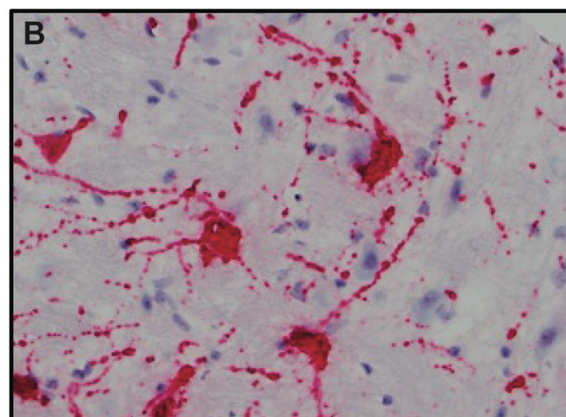

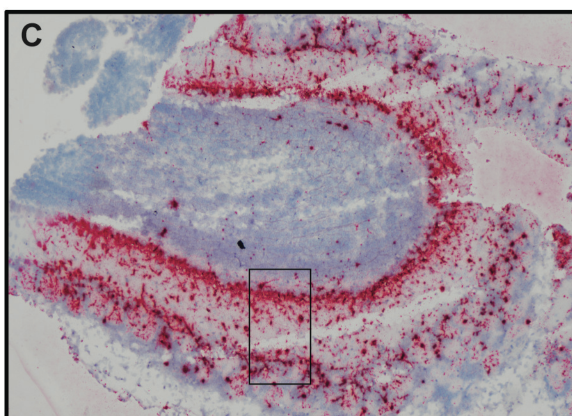

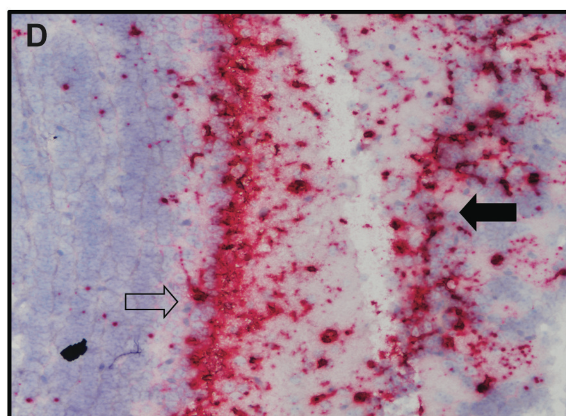

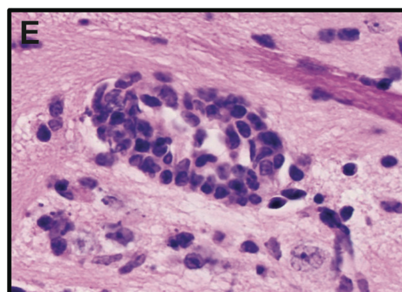

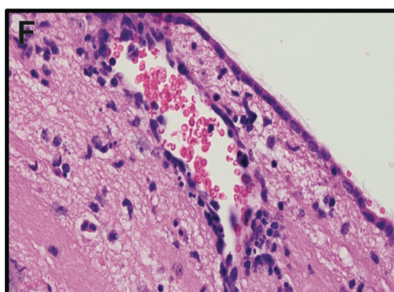

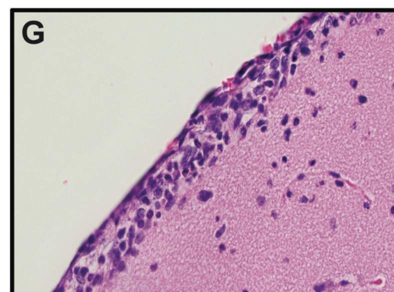

bioRxiv preprint doi: https://doi.org/10.1101/2021.11.15.468761; this version posted November 17, 2021. The copyright holder for this preprint (which was not certified by peer review) is the author/funder, who has granted bioRxiv a license to display the preprint in perpetuity. It is made available under aCC-BY-NC-ND 4.0 International license.

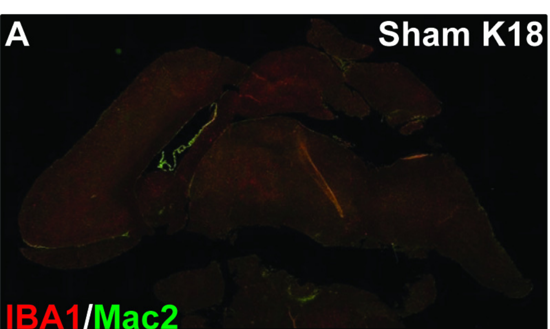

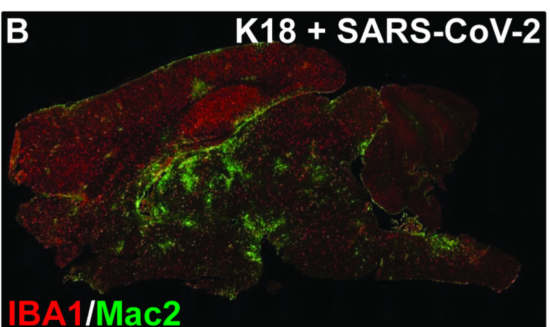

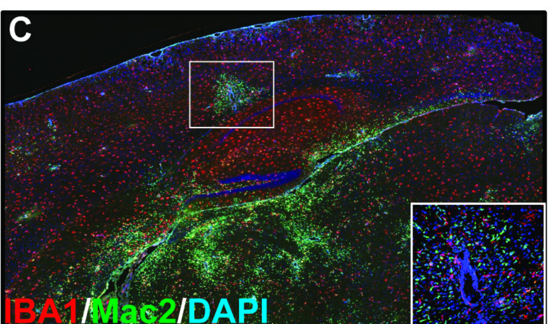

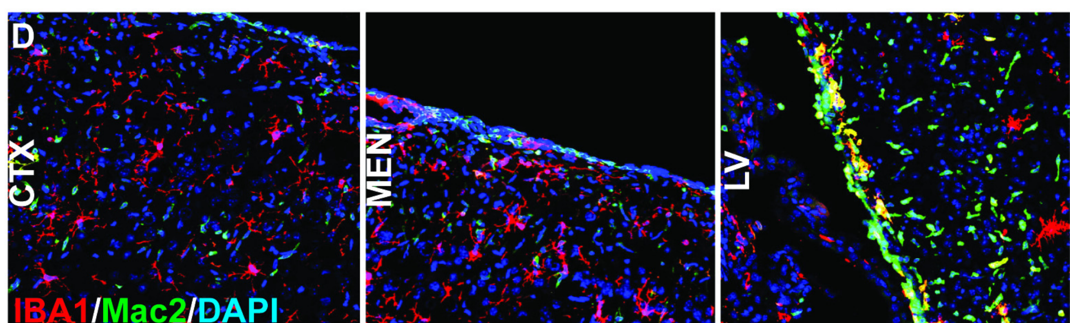

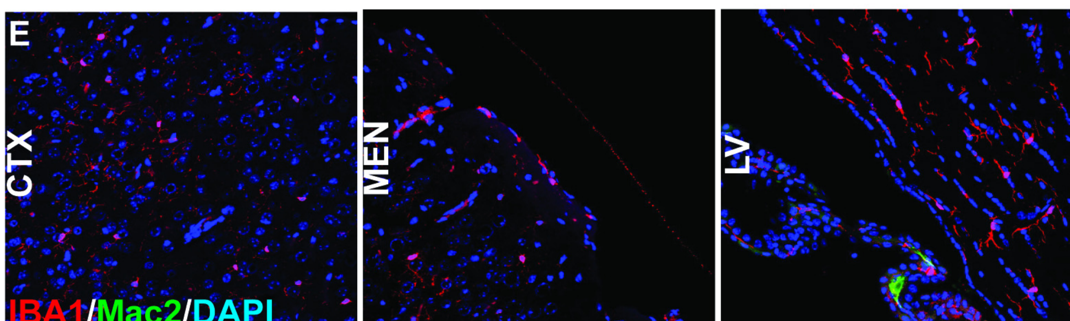

bioRxiv preprint doi: https://doi.org/10.1101/2021.11.15.468761; this version posted November 17, 2021. The copyright holder for this preprint (which was not certified by peer review) is the author/funder, who has granted bioRxiv a license to display the preprint in perpetuity. It is made available under aCC-BY-NC-ND 4.0 International license.